

Static and transient vacuolation in protein-based coacervates induced by charged amino acids

Received: 26 March 2024

Accepted: 19 June 2025

Published online: 01 July 2025

Zhenhua Li^{1,4}, Qing Liu^{1,4}, Han Ding¹, Zhuojun Meng¹, Qi-Hong Zhao², Nan-Nan Deng^{2,3}✉ & Lifei Zheng¹✉

Vacuolation is a common phenomenon observed in many subcellular membrane-less organelles, such as paraspeckles, granules and nucleoli. Previous work suggests that such dynamic sub-structuration can be a result of charge disproportion at super-stoichiometric ratios of the assembling component. In this work, we demonstrate that other than remodeling the large coacervate-constituting components, the introduction of small charged motifs, amino acids, can also lead to the formation of static vacuoles in the coacervate droplets. Furthermore, we find that transient vacuolation can be induced when the charged amino acid (L-aspartic acid) is in situ produced in the coacervate droplets. The transient vacuoles can be tuned in lifetimes and initiated repeatedly, which highly resembles the ubiquitous dissipative assemblies in living systems that require a continuous supply of energy or matter. Therefore, our work may suggest an avenue to understand the sub-structuration within subcellular membrane-less organelles.

While eukaryotic cells and some of their subcellular organelles adopt membrane-bound compartmentalization, a range of endogenous organelles exist in a membrane-less form, such as ribonucleoprotein (RNP) granules, nucleoli and stress granules^{1,2}. These membrane-less organelles (MLOs) are typically organized by the self-segregation of proteins and nucleic acids from the bulk aqueous phase through liquid-liquid phase separation (LLPS)³. Strikingly, such biomolecule-rich condensates are in a liquid-like state, which, together with the membrane-less morphology, promotes rapid structural rearrangement and molecular communication with their surroundings^{4–6}.

In cells, MLOs are found to be strictly related to many subcellular processes, including signaling, gene expression and RNA processing^{1,3,7}. Increasing evidence reveals that such dense biomolecular liquids possess hierarchically organized sub-compartments with distinct compositions, which are believed to facilitate spatiotemporal control over complex biochemical processes^{8–13}. For example, under environmental stress, cytoplasmic stress granules with a dense protein-rich core and a more fluidic shell are produced in cells and

dynamically exchange substances with the cytosol^{14–16}. Nucleolus, on the other hand, exhibits a nested architecture owing to its major role in ribosome biogenesis, a process that involves multiple orchestrated steps in distinct and immiscible sub-compartments^{10,17}. Droplets displaying a hollow morphology have also been broadly distinguished in nuclear and germ granules^{18–21}. For instance, HSP70 chaperones are found to facilitate RNA-binding-deficient protein TDP-43 to form intranuclear spherical shells, a structure that is speculated to be precursors of TDP-43 aggregates found in many age-related neurodegenerative diseases²¹. Since HSP70 chaperone is crucial for the shell formation, the transition between a shell and a homogeneous droplet can be reversibly converted by controlling the availability of adenosine triphosphate. Considering the large number and diverse functions of MLOs, continuous efforts are still called for to uncover additional regulatory mechanisms used by cells, which can be challenging but is of pivotal importance to shed light on the molecular origin of some devastating diseases (such as amyotrophic lateral sclerosis and Alzheimer's disease)^{22,23}.

¹Wenzhou Institute, University of Chinese Academy of Sciences, Wenzhou, China. ²School of Chemistry and Chemical Engineering, Shanghai Jiao Tong University, Shanghai, China. ³Shanghai Jiao Tong University Sichuan Research Institute, Chengdu, Sichuan, China. ⁴These authors contributed equally: Zhenhua Li, Qing Liu. ✉e-mail: n.deng@sjtu.edu.cn; zhenglif@ucas.ac.cn

Many synthetic coacervate models have been proposed to explore the distinct features of MLOs^{24–27}. For example, active coacervate microdroplets have been reported that are regulated by chemical fuels, exhibiting a feature that highly resembles the ubiquitous processes in living systems^{28–30}. These droplets reside in an out-of-equilibrium state and resolve when the fuel is discontinued^{31–36}. To mimic and understand the hierarchical organization of sub-compartments in MLOs, researchers have constructed coacervate droplets that display multiphase sub-structures^{37–41}. Notably, vacuole formation was observed in a couple of artificial systems during coacervate dissolution^{42–53}. For instance, Banerjee and coworkers reported that RNA could trigger a reentrant phase transition of arginine-rich peptides, and a continuous influx of the constituting RNA to pre-formed condensates could induce vacuole formation and eventually lead to condensate dissolution^{44,45}. Aided by molecular dynamics simulation, they showed that at compositionally disproportionate conditions, the peptide or RNA could form anisotropic structures (such as tadpoles) that were further assembled into vesicular topologies. Considering the active transcription of RNA in cells, it was proposed as one of the plausible explanations for the dynamic vacuolation within MLOs. In the Liedl and Walther group, transient vacuolation was identified in all-DNA condensates when enzyme-induced DNA degradation was triggered from the inside^{30,50,51,53}. The restriction enzymes were enclosed in the droplets via either passive migration from the outside or kinetic entrapment during coacervate formation. The constituting DNA strands were cleaved into small fragments by the enclosed enzymes, and an osmotic pressure was created inside coacervates, which led to the transport of water into droplets and the initiation of vacuoles. Due to the high affinity of the restriction enzymes to the DNA backbone, vacuoles were continuously initiated until the droplets were completely dissolved. Recently, Boekhoven and coworkers reported a similar spherical shell formation during the dissolution of chemically fueled droplets⁵⁴. Such a constituting motif-elimination-related route may suggest a possible mechanism for the formation of vacuolated structures in cells. On the other hand, it has to be noted that many MLOs are intrinsically active and can internally generate motifs that may alter the local composition (other than MLO-

constituting components) and arrangement². Therefore, studies in this direction may offer insights into understanding the rearrangement of subcellular organelles, but many aspects of this phenomenon remain unclear or elusive, for example, the influence of biochemical processes and other biomolecules.

In this work, we construct an enzymatically active coacervate to study how the *in situ* biochemical process influences the sub-structuration of coacervates (Fig. 1). We first demonstrate that the addition of charged amino acids (AAs: L-aspartic acid, glutamic acid or lysine) to coacervate droplets can induce the formation of static internal vacuoles, showing a similar effect as that induced by monotonically increasing the assembling components or adjusting the system pH. Next, we report that transient vacuolation can be initiated via *in situ* production of L-aspartic acid in the coacervate droplets, by which the vacuoles can be tuned in lifetimes and initiated repeatedly. The enzymatic reaction-mediated dynamic rearrangement in coacervates highly resembles the out-of-equilibrium vacuolation in endogenous organelles. This similarity suggests that our system may serve as a promising model to study non-equilibrium sub-structuration in MLOs.

Results and discussion

Electrostatic interactions play a pivotal role in the process of LLPS, which is critical for the formation of biomolecular condensates. Herein, we engineered a supercharged unfolded polypeptide bearing 72 lysines (K72) and a green fluorescent protein possessing 30 negative charges (GFP30)^{55–57}. Their structural integrity was verified by sodium dodecyl sulfate-polyacrylamide gel electrophoresis (SDS-PAGE) and matrix-assisted laser desorption/ionization-time of flight mass spectrometry (MALDI-TOF MS, Fig. S1). To facilitate tracking the distribution within the condensates, K72 was labeled with a red fluorescent dye Cy5.

The engineered components were subsequently mixed in a phosphate buffer (PB: 3.75 mM Na₂HPO₄, 1.25 mM NaH₂PO₄, pH = 7.4) and analyzed using fluorescence microscopy. By systematically varying the charge ratio of the assembling components and salt concentration, we plotted the phase diagram. As shown in Fig. 2a, at super-stoichiometric ratios ($C_{\text{negative charge}}/C_{\text{positive charge}} < 0.5$) or in the presence of high concentrations of NaCl ($C_{\text{NaCl}} > 120$ mM), no coacervate

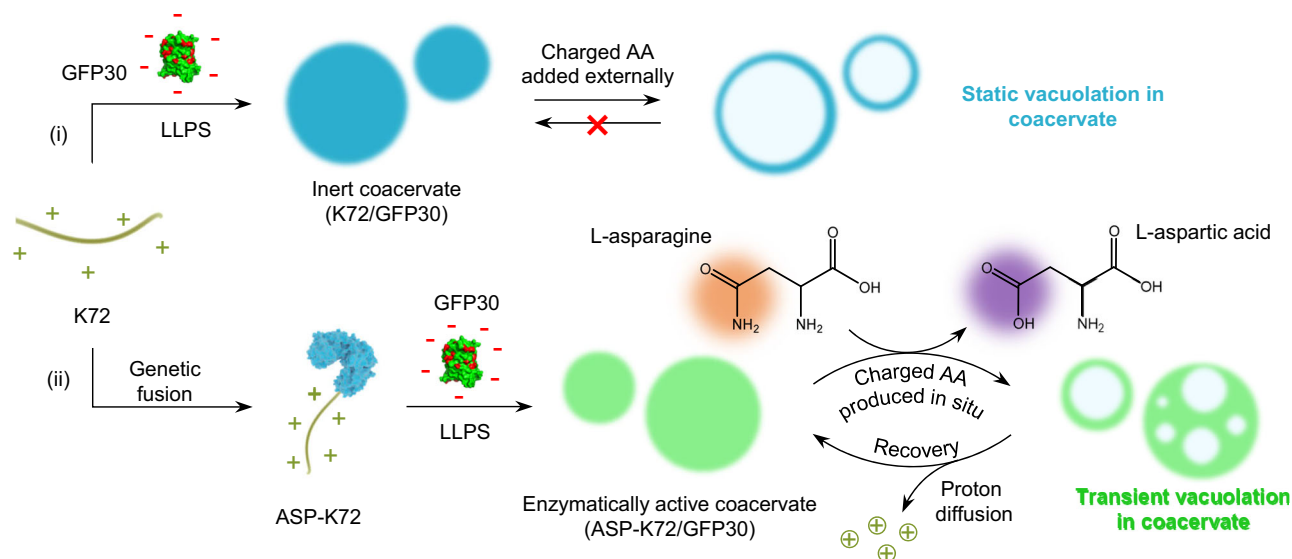


Fig. 1 | Illustration of the static and transient vacuolation induced in protein-based coacervates. In route (i), supercharged unfolded polypeptide bearing 72 positive charges (K72) is engineered and complexed with negatively charged GFP30 into inert coacervate microdroplets via LLPS. The following introduction of charged AAs (L-aspartic acid, glutamic acid or lysine) induces charge access that leads to the formation of static vacuoles in K72/GFP30 droplets. In route (ii), a

biological enzyme, L-asparaginase (ASP), is first fused to K72 via genetic engineering and then condensed with GFP30, producing enzymatically active coacervates. The addition of the substrate, L-asparagine, *in situ* generates L-aspartic acid that initiates transient vacuolation in ASP-K72/GFP30 droplets. The transient vacuoles can be initiated for many cycles via the repeated introduction of L-asparagine.

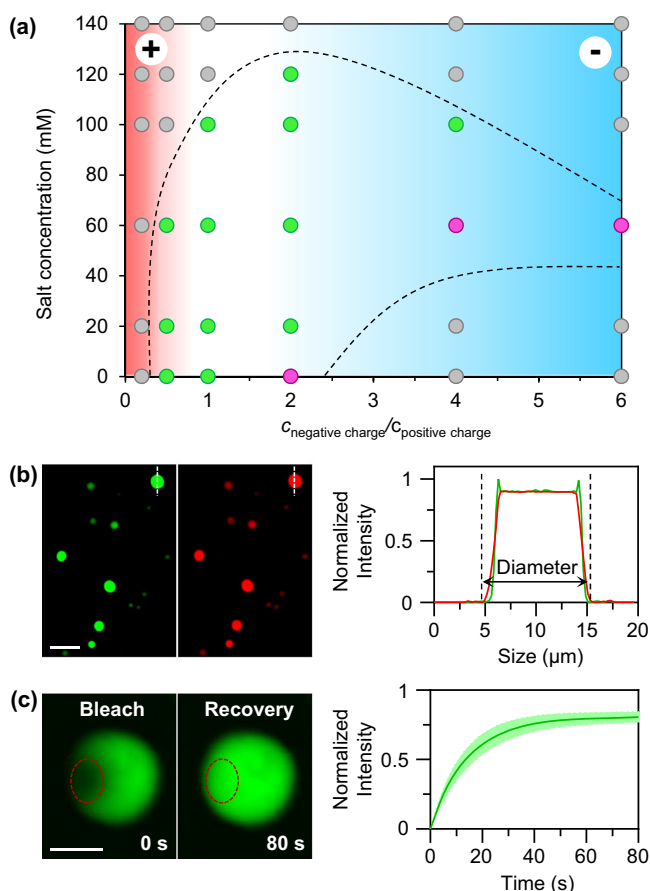


Fig. 2 | Characterization of K72/GFP30 coacervates. **a** The phase diagram of K72/GFP30 at different charge ratios and salt concentrations. Green and rose dots indicate conditions under which condensate droplets or shells are observable, respectively, while gray dots indicate conditions where no assembly is observed. In all measurements, the positive charge concentration is 3 mM while the negative charge concentration is varied from 0.6 to 18 mM. The dashed lines are the approximate phase boundaries and are meant as a guide to the eye. **b** Fluorescence microscopy images and the fluorescence intensity profiles across the representative coacervate microdroplet of K72/GFP30 coacervates under GFP (left) and Cy5 (right) channels ($C_{\text{positive charge}} = C_{\text{negative charge}} = 3$ mM, PB, 60 mM NaCl). K72 was labeled with Cy5. Scale bar: 20 μm . **c** FRAP measurement and the corresponding intensity time trace for GFP30 showing the fluorescence recovery of GFP in K72/GFP30 microdroplet. The red circles indicate the bleaching region. Scale bar: 5 μm . Measurements in **c** were performed using triplicate samples, and the averaged results with standard deviation were presented. Source data are provided as a Source Data file.

microdroplets were observed, a phenomenon that was reported in previous work^{44,45}. In contrast, at selected conditions (i.e., $C_{\text{negative charge}} = C_{\text{positive charge}} = 3$ mM, $C_{\text{NaCl}} = 60$ mM), K72/GFP30 microdroplets displayed a spherical morphology with GFP30 (green) and K72 (red) homogeneously distributed throughout the droplets (Fig. 2b). This observation is particularly intriguing given that GFP30 lacks the typical flexible strand-like structure often associated with promoting coacervation^{26,58}. Fluorescence recovery after photobleaching (FRAP) measurement showed that the fluorescence intensity of GFP gradually recovered ~81% in 80 s at 25 °C, confirming the liquid-like feature of the droplets (Fig. 2c). Under specific non-neutral conditions, we also observed the formation of vesicle-like condensates characterized by a water-filled lumen and a thin outer membrane containing coacervate material, as indicated by the rose dots in Fig. 2a^{44,45}.

To further explore the vacuolation phenomenon, spherical coacervates were prepared at equal charge conditions ($C_{\text{positive charge}} = C_{\text{negative charge}} = 3$ mM, PB, 68.5 mM NaCl). We then examined whether

vacuolated droplets could be generated by incrementally increasing the concentration of either component within the coacervates, as previously reported^{44–47}. By using the reported setup (Fig. S2)²⁸, we indeed observed a transformation from droplets to vesicles upon increasing the concentration of either K72 or GFP30 (Fig. S3a–j). Notably, FRAP measurements revealed a decrease in the fluidity of the biopolymers at the droplet rim, with fluorescence recovery reaching ~55% within 60 s. (Fig. S3k–n). This behavior paralleled observations made in membranized alginate/silk fibroin coacervate vesicles, suggesting an enhancement in the interactions between protein chains within the condensates^{46,47}. Moreover, electrophoretic mobility measurements showed a sharp decrease when GFP30 was monotonically increased while K72 imposed an opposite effect (Fig. S3o), implying that the low-density phase (vacuole) within the droplets arose from the charge excess at super-stoichiometric ratios as reported in previous work^{44–47}.

Aside from assembling macromolecules, pH has also been reported to induce vacuolation within protein-based coacervates by modulating the $[\text{NH}_3^+]:[\text{COO}^-]$ charge ratio^{46,47}. We indeed observed static vacuoles in K72/GFP30 coacervates at non-neutral pH conditions by titrating the solution with HCl or NaOH (Fig. S4). Considering the diversity and the significant biological role, we proceeded to evaluate if AAs could induce a similar behavior in preformed coacervates (Fig. 1, route i). The results are shown in Fig. 3 and Figs. S5–S9. It was found that the introduction of 8 mM L-aspartic acid created vacuoles and that their size was gradually increased and stabilized after 300 s (Fig. 3a). In the presence of 10 mM L-aspartic acid, a vesicle-like structure was formed instantly, and the rim was much thinner than that formed at 8 mM L-aspartic acid (Fig. 3b, c). Analysis of the effect of L-aspartic acid concentration on the vacuole size and percentage of vacuolated droplets (vacuole rate) showed that they were positively correlated: while no vacuolation was observed in the presence of 5 mM L-aspartic acid, an increase to 8 and 10 mM L-aspartic acid created vacuoles of 1.8 ± 1.6 μm and 4.7 ± 3.5 μm , respectively, with vacuole rates of ~57% and ~74%, respectively (Fig. 3d). An increase in the concentration of L-aspartic acid to 20 mM completely dissolved the droplets (Fig. S6). Fluorescence microscopy images showed that the signals from GFP30 and K72 overlapped at the rim (Fig. 3b), suggesting the colocalization of K72 and GFP30. Besides, compared to the droplets, the fluorescence recovery of the rim was slower after bleaching (~50% in 100 s for the rim vs. ~81% in 80 seconds for the droplet, Figs. 2c, 3e), indicating that L-aspartic acid could display a similar effect in restricting the mobility of the constituting biopolymers in the vacuolated structures.

To gain more insights into the vacuolation mechanism, a series of control experiments were carried out. It was found that the formation of vacuoles could also be triggered via the introduction of glutamic acid (Fig. S7) or lysine (Fig. S8). On the contrary, the addition of alanine or proline (10 mM) imposed no obvious influence on the morphology of the microdroplets (Fig. S9). Further quantification of the partitioning efficiency of L-aspartic acid in K72/GFP30 coacervates yielded a value of ~223, indicating a preferential accumulation of L-aspartic acid within the polyelectrolyte coacervates, akin to other charged motifs, such as Mg^{2+} , nucleotides and RNA^{59,60}. The concentrated L-aspartic acid is anticipated to enhance the $[\text{NH}_3^+]:[\text{COO}^-]$ charge ratio and the concomitant surface potential through the protonation of $-\text{COO}^-$ groups^{46,47}. We measured the electrophoretic mobility as a function of L-aspartic acid concentration and indeed observed a charge inversion from negative to positive at around 8 mM L-aspartic acid (Fig. 3f), consistent with the fluorescence microscopy observations that showed no vacuoles until this concentration was reached (Figs. 3a and S5)^{44,45}. Similarly, vacuoles were identified in the presence of 8 mM lysine (Fig. S8d), which matched the electrophoretic mobility measurement that exhibited a sharp drop at ~8 mM lysine (Fig. 3f). The lysine-induced vacuolation could be attributed to the deprotonation of $-\text{NH}_3^+$ on K72, which led to a decrease in the $[\text{NH}_3^+]:[\text{COO}^-]$ charge ratio⁴⁶. On the contrary, when K72/GFP30 was treated with neutralized

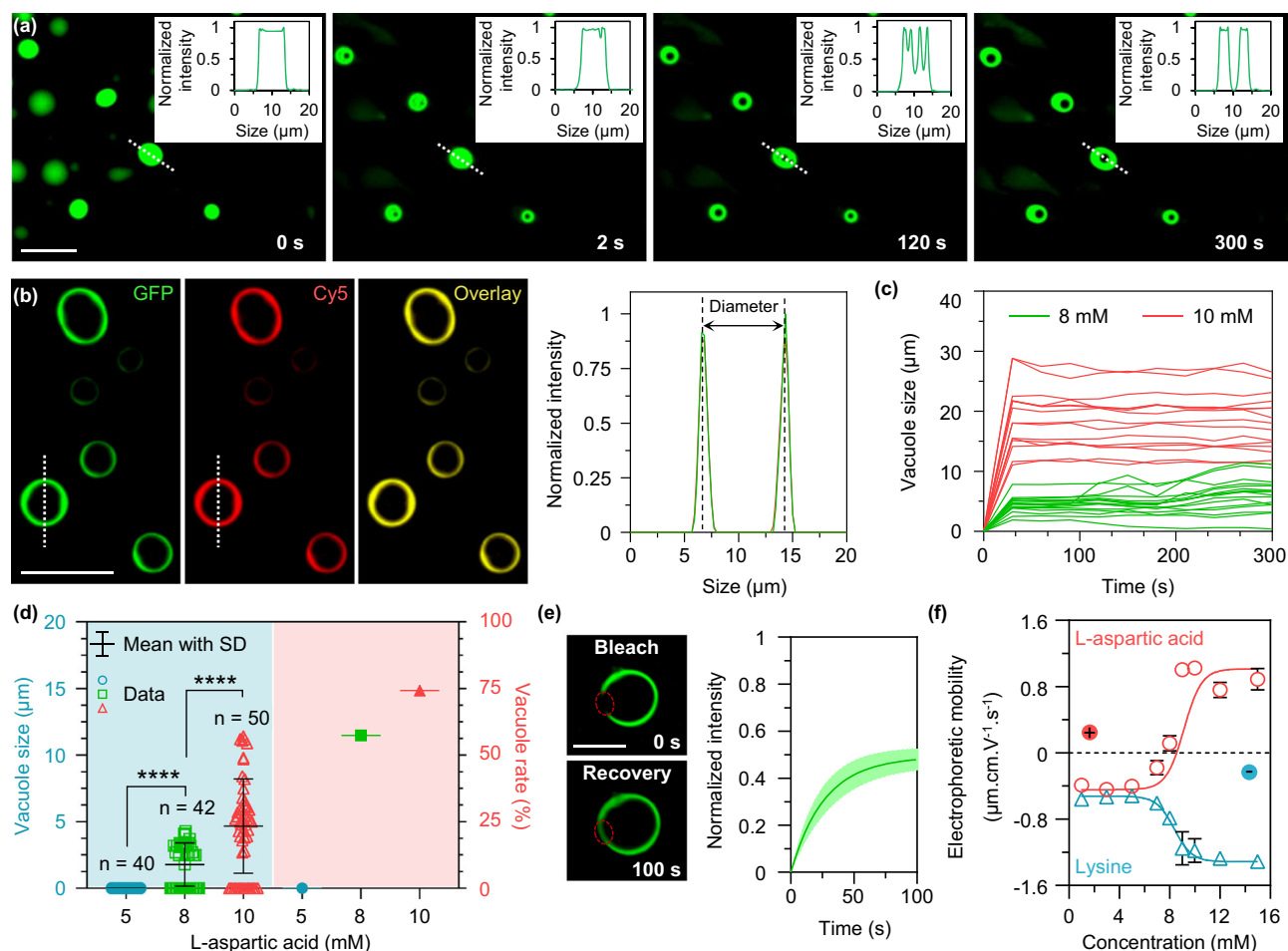


Fig. 3 | Characterization of the static vacuoles triggered in K72/GFP30 coacervates upon the introduction of L-aspartic acid. **a** Fluorescence microscopy images and the corresponding intensity profiles (insets) of K72/GFP30 coacervates at different time points (0, 2, 120, and 300 s) showing the time-dependent evolution of vacuoles after the introduction of 8 mM L-aspartic acid. Scale bar: 20 μm . **b** Fluorescence microscopy images and the corresponding plot profiles of K72/GFP30 droplet in the presence of 10 mM L-aspartic acid in 2 s. K72 was labeled with Cy5. Scale bar: 10 μm . **c** Traces of individual K72/GFP30 coacervates in the presence of 8 mM ($n = 16$) or 10 mM ($n = 15$) L-aspartic acid showing the size evolution of vacuoles in 300 s. **d** The variation in vacuole size and percentage of vacuolated

droplets in the presence of 5, 8, and 10 mM L-aspartic acid after 300 s. The blue shading indicates the data fall into the left y axis while the red shading indicates the data fall into the right y axis. (exact P value: 5 vs. 8 $P = 9.049\text{E}-10$, 8 vs. 10 $P = 4.747\text{E}-6$). **e** FRAP measurement images and the corresponding time trace of intensity at the rim in the presence of 10 mM L-aspartic acid. The red circles indicate the bleaching region. Scale bar: 10 μm . **f** Evolution of the electrophoretic mobility of K72/GFP30 coacervates in the presence of varying concentrations of L-aspartic acid or lysine. Measurements in (**e**, **f**) were performed using triplicate samples, and the averaged results with standard deviation were presented. SD: standard deviation. **** $p < 0.0001$. Source data are provided as a Source Data file.

L-aspartic acid (10 mM monosodium L-aspartate), no obvious change in the structure was observed (Fig. S10). These results highlighted the dominant role of charge disproportion induced by the trafficking of protons in the formation of coacervate vacuoles. Moreover, the significantly reduced FRAP value for the vacuolated structures suggested that the mobility of the biopolymers was constrained by the concentrated L-aspartic acid or lysine (Figs. 3e, S8h), a phenomenon commonly observed with other ions or environmental factors (e.g., temperature, shear force)^{48,61–63}. This restriction is believed to counterbalance the osmotic pressure generated within the system, thereby stabilizing the vacuolated structures^{46,47}.

Based on the experimental results and reported literature^{44–47}, the plausible mechanism for vacuole formation within protein coacervates was proposed. The addition of L-aspartic acid or lysine appears to increase the net surface charge by protonating GFP30 or deprotonating K72, respectively and consequently elevates the free energy of K72/GFP30 droplets. The increase in free energy promotes the formation of an additional interface (vacuoles) as a means to lower the overall free energy^{44,45}. The restructuring of the coacervate droplets further leads to an increase in osmotic pressure which is likely due to a concentration

gradient of the charged L-aspartic acid or lysine across the coacervate vesicle, resulting in the ingress of water and concomitant volume expansion of the vacuoles. Furthermore, the enriched L-aspartic acid or lysine may exert effects similar to salting-out ions in the Hofmeister series, which increase the viscosity of the condensates and thereby contribute to the stabilization of the vacuolated structures⁶¹.

It should be noted that the composition of subcellular condensates can be in situ altered because they are typically responsible for certain biochemical processes². Such internal composition change may also reshape the structure of MLOs, a behavior that can be different from that triggered externally^{44–47}. Therefore, we set out to evaluate how the in situ production of charged AAs will influence the structure of coacervate microdroplets.

We selected a catalytic enzyme, L-asparaginase (ASP), which can convert neutral L-asparagine to L-aspartic acid^{64,65}. To promote condensation, we fused ASP to K72 (ASP-K72). The size and structure integrity of the product were verified by SDS-PAGE, MALDI-TOF MS, and circular dichroism (Fig. S11). Analysis of ASP-K72 showed an enzymatic activity of $\sim 1208.5 \text{ U mg}^{-1}$, indicating that the activity of ASP was negligibly influenced by K72.

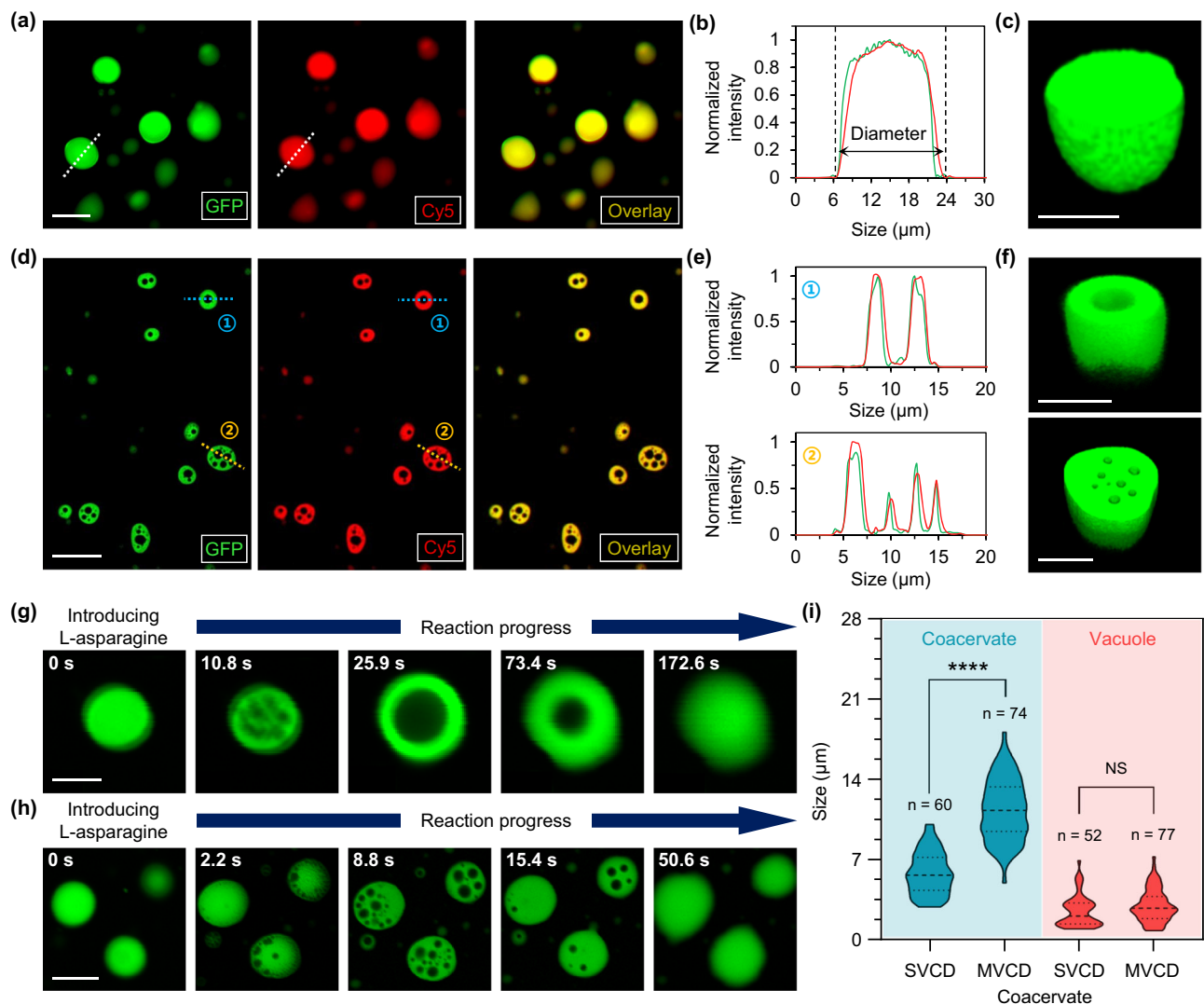


Fig. 4 | Characterization of the transient vacuolization in ASP-K72/GFP30 coacervates induced by in situ production of L-aspartic acid. (a) Fluorescence microscopy images of ASP-K72/GFP30 microdroplets ($C_{\text{positive charge}} = C_{\text{negative charge}} = 3 \text{ mM}$). ASP-K72 was labeled with Cy5. Scale bar: 20 μm . (b) The plot profiles of the microdroplet indicated in (a). (c) 3D reconstruction of an ASP-K72/GFP30 microdroplet. Scale bar: 10 μm . (d) Fluorescence microscopy images of ASP-K72/GFP30 microdroplets 5 s after the introduction of 10 mM L-asparagine. Scale bar: 20 μm . (e) The corresponding plot profiles of the microdroplets indicated in (d). (f) 3D reconstruction of an SVCD and an MVCD in the presence of 10 mM L-asparagine.

Scale bar: 10 μm . Fluorescence microscopy images of ASP-K72/GFP30 microdroplets showing the time-dependent structural evolution in (g) SVCD and (h) MVCD after the introduction of 10 mM L-asparagine. Scale bar: 3 μm in (g) and 20 μm in (h). (i) Comparison of the vacuole (at the coarsening phase) and coacervate sizes between SVCD and MVCD upon the introduction of 10 mM L-asparagine. (exact P value: SVCD vs. MVCD in coacervate size $P < 0.0001$, SVCD vs. MVCD in vacuole size $P = 0.0572$.) Statistical significance: ns: statistically non-significant; **** $p < 0.0001$. Source data are provided as a Source Data file.

Next, the ability of ASP-K72 to form coacervate with GFP30 was evaluated ($C_{\text{positive charge}} = C_{\text{negative charge}} = 3 \text{ mM}$, the positive charge here and in the following work indicates charges from K72 only unless otherwise stated). As shown in Figs. 4a–c and S12, similar spherical microdroplets were produced, and both ASP-K72 and GFP30 were homogeneously dispersed across the condensates (ASP-K72 was labeled with Cy5). Investigation of the phase diagram revealed that the formation of coacervate followed a similar tendency as K72/GFP30, and FRAP measurement confirmed the mobility of GFP30 in the coacervate (~83% in 80 s, Fig. S12c, d). It was also found that static vacuoles could be produced in ASP-K72/GFP30 droplets when 10 mM L-aspartic acid was introduced (Fig. S13).

Subsequently, we monitored the morphology evolution of the complex by introducing 10 mM substrate (L-asparagine) to pre-assembled ASP-K72/GFP30 coacervates ($C_{\text{positive charge}} = C_{\text{negative charge}} = 3 \text{ mM}$, PB, 68.5 mM NaCl). Strikingly, transient vacuolization was observed in the droplets, and a typical nucleating-coarsening-

dissolving process was followed^{43,48}. As shown in Fig. 4 and Supplementary Movie S1,2, multiple small vacuoles were first nucleated upon the addition of L-asparagine. The small vacuoles then coarsened into big ones through fusion and ripening. Afterward, the big vacuoles gradually shrunk and eventually dissolved. Two types of droplets at the coarsening phase were distinguished, including single-vacuole-containing droplets (SVCD) and multiple-vacuole-containing droplets (MVCD). Quantitative analysis revealed that the number of vacuoles in coacervates was positively related to the droplet size⁴⁸. As shown in Fig. 4i, SVCD had a size of $5.9 \pm 1.9 \mu\text{m}$ while that for MVCD was $11.4 \pm 2.7 \mu\text{m}$. Despite the obvious difference in the condensate size, the vacuoles produced in the two types of coacervates displayed a similar size ($2.3 \pm 1.3 \mu\text{m}$ for SVCD and $2.6 \pm 1.3 \mu\text{m}$ for MVCD, Fig. 4i). A snapshot of the droplets at the vacuolated state (5 seconds after the introduction of L-asparagine) showed that the red fluorescence from ASP-K72 overlapped with the green one from GFP, and both signals colocalized at the rim, indicating that the vacuoles were depleting of

ASP-K72 and GFP30 (Fig. 4d, e). Z-stack analysis using confocal fluorescence microscopy showed the existence of internal lumens within both SVCDs and MVCDs (Fig. 4f). Control experiments with K72/GFP30 in the presence of 10 mM L-asparagine or with ASP-K72/GFP30 in the presence of 10 mM D-asparagine revealed that no obvious change in coacervate structure was induced (Fig. S14).

The above results suggested that the initiation of vacuoles in ASP-K72/GFP30 coacervates was a result of the ASP-catalyzed production of L-aspartic acid which protonated the carboxylate groups on GFP30 and eventually induced a charge excess by increasing $[\text{NH}_3^+]:[\text{COO}^-]$ charge ratio, showing a similar effect as that to K72/GFP30 droplets. To confirm this hypothesis, we used a commercial fluorescent pH probe

(pHrodo™ Red) to in situ trace the pH change within ASP-K72/GFP30 droplets upon the introduction of L-asparagine. This probe displays weak fluorescence at neutral pH but becomes increasingly fluorescent as the pH drops. We also recorded the GFP30 signal (green) for comparison. As shown in Figs. 5a and S15, along with the vacuole formation, an obvious jump in the red signal intensity was observed after the introduction of L-asparagine (10 mM) while the green signal from GFP30 only showed irregular variation over time, implying a pH drop in coacervates. The relative fluorescence intensity (red/green) confirmed the profound influence on the pH probe compared to GFP30. After reaching an intensity peak, the signal from the probe was restored to the starting state, which meant that the pH was increased

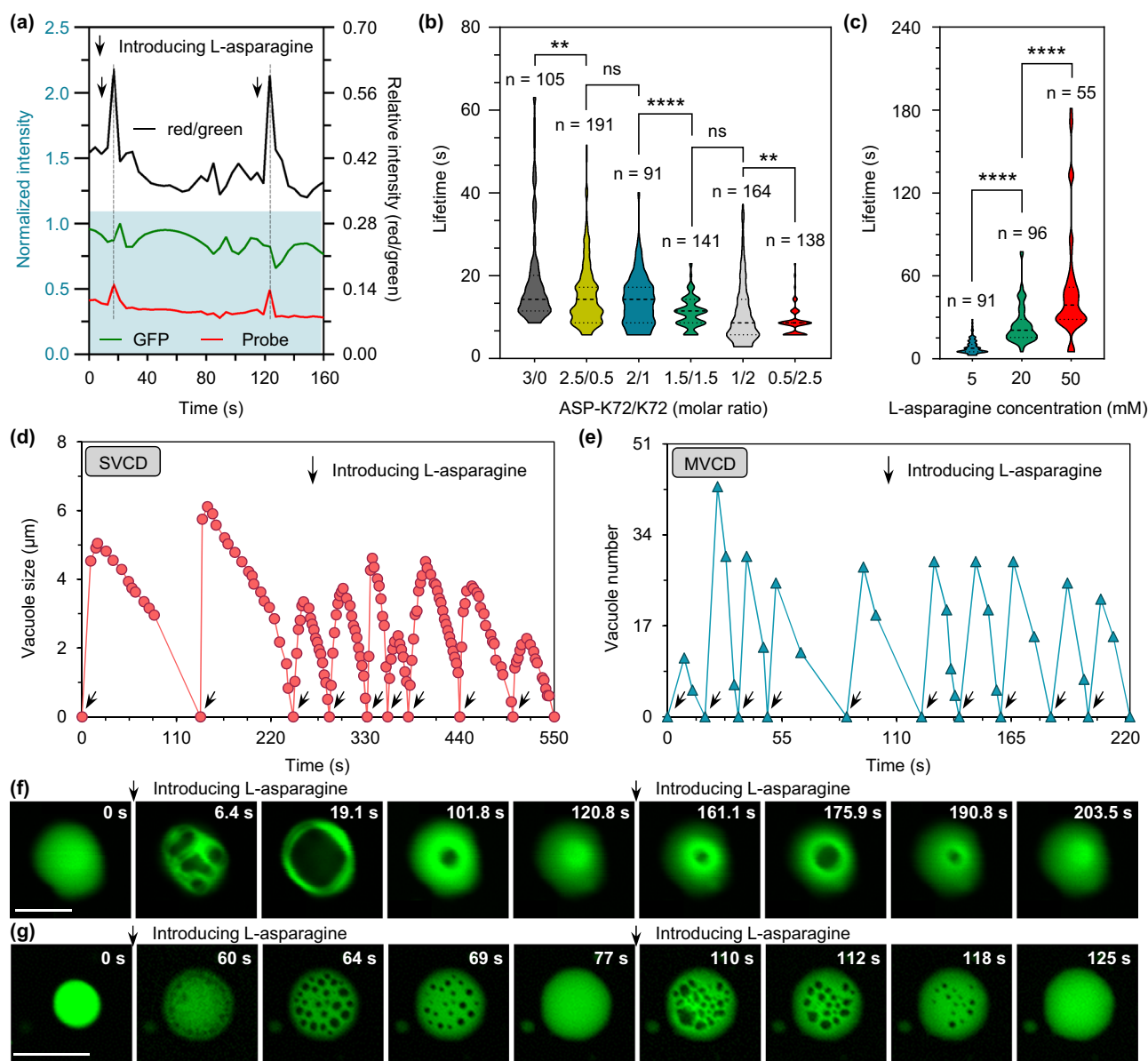


Fig. 5 | Analysis of the L-asparagine-triggered transient vacuolation within ASP-K72/GFP30 microdroplets. a In situ fluorescence intensity evolution of the probe (pHrodo™ Red) and GFP30 (green) in response to L-asparagine (10 mM) for two cycles. The blue shading indicates the two curves fall into the left y axis. **b** The relationship between vacuole lifetime and ASP-K72/K72 ratio determined from fluorescence microscopy images. In all samples: $c_{\text{positive charge}} = c_{\text{negative charge}} = 3 \text{ mM}$; L-asparagine: 10 mM. (exact P value: 3/0 vs. 2.5/0.5 $P = 1.0674\text{E-}3$, 2.5/0.5 vs. 2/1 $P = 0.10722$, 2/1 vs. 1.5/1.5 $P = 3.62\text{E-}5$, 1.5/1.5 vs. 1/2 $P = 0.5764$, 1/2 vs. 0.5/2.5 $P = 6.21\text{E-}3$). **c** The relationship between vacuole lifetime and L-asparagine

concentration (5, 20, and 50 mM). (exact P value: 5 vs. 20 $P < 0.0001$, 20 vs. 50 $P = 9.039\text{E-}8$). ns, statistically non-significant; ** $p < 0.01$; **** $p < 0.0001$. **d** Evolution of vacuole size in SVCD upon repeated introduction of L-asparagine (10 mM). **e** Evolution of vacuole number in MVCD upon repeated introduction of L-asparagine (10 mM). Source data are provided as a Source Data file. **f** Representative fluorescence microscopy images of SVCD upon the introduction of L-asparagine (10 mM) for two cycles. Scale bar: 3 μm. **g** Representative fluorescence microscopy images of MVCD upon the introduction of L-asparagine (10 mM) for two cycles. Scale bar: 20 μm.

again. Concomitantly, the vacuoles disappeared (Fig. S15). We also determined the influence of L-asparagine on the two fluorescent signals (pHrodo™ Red and GFP30) in K72/GFP30, and no obvious change was detected while the droplet displayed no obvious structural alteration (Fig. S16a, c). On the other hand, the introduction of L-aspartic acid induced a significant increase in the fluorescence intensity of the probe (Fig. S16b, d), which could be due to the significantly decreased pH induced by enriched L-aspartic acid.

Taken together, we propose that the initiation of vacuoles can be a result of the in situ pH drop caused by the ASP-catalyzed production of L-aspartic acid in ASP-K72/GFP30 coacervates. Since the majority of ASP is located in the droplets, the L-asparagine-to-L-aspartic acid conversion is anticipated to be mainly carried out inside the coacervates, which produces a high transient concentration of protons that initiates vacuoles within the droplet by inducing a charge excess through protonating -COO^- groups^{46,47}. On the other hand, the environmental phosphate buffer (pH = 7.4) can neutralize the generated protons and recover the pH within the coacervates, restoring the original droplet structure. Besides, the disappearance of vacuoles implied that L-asparagine was not fully converted by ASP as 10 mM L-aspartic acid was found to induce static vacuoles in ASP-K72/GFP30 coacervates (Fig. S13). We characterized the activity of ASP-K72 in the bulk solution and found it dropped from $-1208.5 \text{ U mg}^{-1}$ to -515 U mg^{-1} in the presence of 20 mM L-aspartic acid (Fig. S17). Considering the high partitioning efficiency of L-aspartic acid in coacervates (~ 223), the enzymatic reaction could be far less efficient when vacuoles were produced. Such an adverse effect was also identified in other enzyme-catalyzed systems^{66,67}. FRAP measurement of ASP-K72/GFP30 droplet after one transient cycle showed a value of $\sim 75\%$ in 200 s (Fig. S18), which was between that from the intact droplet ($\sim 83\%$ in 80 s) and the static rim ($\sim 50\%$ in 100 s). Such observation might also suggest a lower L-aspartic acid concentration compared to that in the static vacuolated structures. Therefore, these two factors (proton diffusion and restricted production) caused a pH increase that led to the disappearance of vacuoles in ASP-K72/GFP30 droplets.

We also investigated the influence of ASP-K72 concentration on vacuolation dynamics by preparing coacervates containing varying ratios of ASP while keeping the total charges constant ($C_{\text{positive charge}} = C_{\text{negative charge}} = 3 \text{ mM}$; K72: ASP-K72 = 0.5: 2.5, 1: 2, 1.5: 1.5, 2: 1, 2.5: 0.5 and 3: 0). After the introduction of L-asparagine (10 mM), transient vacuoles were induced in all coacervates in 5 seconds except those without ASP-K72 (K72/GFP30, Figs. S14, S19). Analysis of the vacuole lifetime (from nucleating to dissolving) showed that it increased with the enzyme ratio in the coacervates (Fig. 5b). The lifetime was enhanced from $6.6 \pm 2.5 \text{ s}$ to $14.5 \pm 9.2 \text{ s}$ when the K72: ASP-K72 ratio was switched from 2.5: 0.5 to 0: 3 (the lifetimes indicated an average value from both SVCD and MVCD). These observations confirmed that the initiation of vacuoles resulted from the ASP-catalyzed production of L-aspartic acid in ASP-K72/GFP30 coacervates.

In addition to the enzyme ratio, we found the vacuole lifetime could be readily tuned by L-asparagine concentration. As shown in Figs. 5c, S20, the lifetime was $7.3 \pm 4.4 \text{ s}$ in the presence of 5 mM L-asparagine, and it was enhanced to $20.7 \pm 11.9 \text{ s}$ and $42.3 \pm 34 \text{ s}$ when 20 mM and 50 mM L-asparagine was added. Particularly, we found that 5 mM L-asparagine triggered vacuolation in ASP-K72/GFP30, a concentration that was much lower than that required to induce static vacuoles in K72/GFP30 (8 mM L-aspartic acid). We determined the partitioning efficiency of L-asparagine and found it reached ~ 181 , demonstrating that L-asparagine was also preferentially accumulated in ASP-K72/GFP30. Therefore, we attributed the different behavior to the in situ production of L-aspartic acid within ASP-K72/GFP30 coacervates, which could generate protons with a transient high concentration surpassing that required for vacuole formation. Following proton diffusion and restriction of enzyme activity led to the pH recovery and consequently vacuole disappearance in ASP-K72/GFP30.

Besides, transient vacuolation was even identified when L-asparagine reached 50 and 200 mM (Figs. 5c, S21), a concentration that was significantly higher than that required to dissolve the droplets (20 mM L-aspartic acid, Fig. S6). Moreover, we also found that the transient vacuolation could be initiated multiple times when the substrate (10 mM) was added repeatedly in both SVCD (Fig. 5d, f) and MVCD (Fig. 5e, g). These observations confirmed that the enzyme activity was suppressed and that the repeated addition of the substrate (L-asparagine) could boost the enzyme activity and enable the system to overcome the threshold for vacuolation readily^{66,67}.

In summary, we demonstrate that the addition of small charged AAs to preassembled coacervate microdroplets can trigger the formation of static vacuoles by inducing a charge excess, an effect that has been described via monotonically increasing the assembling macromolecules or adjusting the system pH. More importantly, we showcase an enzymatically active coacervate model that displays non-equilibrium vacuolation. We demonstrate that the transient vacuolation is caused by the pH change caused by the trafficking of the in situ-generated protons from L-aspartic acid. The vacuolation can be repeatedly initiated through the introduction of the substrate while the lifetime can be readily tuned with the enzyme or the substrate concentrations, a feature significantly reminiscent of biological processes that are sustained by a non-stop influx of matter and energy^{68–70}. Considering the prominent biological roles of AAs in living systems, it is therefore believed that this system can serve as a promising model in elucidating the sub-structuration in organelles and, more fundamentally, the intrinsic processes in living organisms.

Methods

Production of K72 and ASP-K72

K72 and ASP-K72 were produced by following a reported procedure⁵⁶. Briefly, *E. coli* BLR (DE3) cells were transformed with pET-25b expression vectors containing K72 or ASP-K72 genes. For protein production, Terrific Broth medium (12 g tryptone and 24 g yeast extract for 1 L) enriched with phosphate buffer (2.31 g potassium phosphate monobasic and 12.54 g potassium phosphate dibasic for 1 L) and glycerol (4 mL per 1 L TB) and supplemented with $100 \mu\text{g mL}^{-1}$ ampicillin, was inoculated with an overnight starter culture to an initial absorption of 0.1 at 600 nm (OD₆₀₀) and incubated at 37 °C at 200 rpm until OD₆₀₀ reached 0.7. Protein production was induced by a temperature shift to 30 °C. Cultures were then continued for a further 16 h incubation. Cells were subsequently harvested by centrifugation ($3580 \times g$, 20 min, 4 °C), resuspended in lysis buffer (50 mM sodium phosphate buffer, pH 8.0, 500 mM NaCl, 5 mM imidazole) and disrupted with a continuous high-pressure cell disrupter (Union-Biotech Ltd., Shanghai). Cell debris was removed by centrifugation ($14,800 \times g$, 60 min, 4 °C). Proteins were purified from the supernatant under native conditions by NGC™ Chromatography Systems (Bio-Rad). The product-containing solutions were further purified by anion exchange chromatography using a heparin column and desalted with ultrapure water. Purified proteins were frozen in liquid N₂, lyophilized, and stored at -20 °C until further use.

Production of GFP30

GFP30 expression and purification followed a reported procedure⁵⁷. Genes were cloned into a pET expression vector (Novagen), and incubated in *E. coli* BL21(DE3)pLysS overnight in LB medium (5 g yeast extract, 10 g peptone, and 10 g sodium chloride for 1 L) at 37 °C at 200 rpm. The solution was inoculated with an overnight starter culture to an initial OD₆₀₀ of 0.1 and incubated at 37 °C at 200 rpm until OD₆₀₀ reached 0.7. Protein overexpressed was induced by Isopropyl β -D-Thiogalactoside (IPTG, 0.5 mM) for 16 h at 25 °C and 200 rpm. Cells were harvested by centrifugation, resuspended in lysis buffer containing 50 mM sodium phosphate buffer (pH 8.0, 500 mM NaCl, 5 mM imidazole) and lysed by continuous high pressure. Proteins were

purified by an NGCTM Chromatography System (Bio-Rad) and concentrated by Millipore water.

Labeling of K72 and ASP-K72 with Cy5

K72 (0.27 μmol) or ASP-K72 (0.14 μmol) was dissolved in 6 mL $\text{Na}_2\text{CO}_3\text{-NaHCO}_3$ (0.1 M, pH 8.5). Then, Cy5 bearing an isocyanate group in 500 μL water was added at a molar ratio of 5/1 (Cy5/K72). The solution was left for reaction at room temperature for 2 h. Then the reaction solution was purified and concentrated with centrifugation filtration against MilliQ water.

Characterization of electrophoretic mobility

The characterization of electrophoretic mobility followed a reported procedure^{45,46}. Briefly, K72/GFP30 coacervates were first preassembled at an equal charge concentration ($c_{\text{positive charge}} = c_{\text{negative charge}} = 3 \text{ mM}$) in PB. Then, concentrated L-aspartic acid or lysine solutions were added to the coacervate solution to make the desired AA concentrations (1, 3, 5, 7, 8, 9, 10, 12 and 15 mM, 500 μL) with the total volume change below 10%, and the electrophoretic mobility was acquired on a dynamic light scattering (DLS) apparatus. Measurements were performed using triplicate samples.

Determination of the partitioning efficiency of L-aspartic acid and L-asparagine

The method to determine the partitioning coefficient of AAs was adopted from the reported work⁷¹. Briefly, K72/GFP30 coacervates were preassembled at an equal charge concentration ($c_{\text{positive charge}} = c_{\text{negative charge}} = 3 \text{ mM}$). Then, concentrated L-aspartic acid or L-asparagine was added to the coacervate solution and gently vortexed, making a final solution of 60 μL containing 10 mM L-aspartic acid or L-asparagine. Afterward, the mixture solution was centrifuged to precipitate the coacervates. The supernatant was carefully removed, and the volume was estimated with a pipette. The volume of the precipitated coacervate was also carefully estimated according to the reported method⁶⁰.

To determine the L-aspartic acid and L-asparagine concentrations in the supernatant, we first used a commercial kit to chemically label L-aspartic acid or L-asparagine of known concentrations (0, 2, 4, 8, and 10 mM) with a phenyl isothiocyanate group. Afterward, the modified L-aspartic acid and L-asparagine were analyzed with a high-performance liquid chromatography equipped with a XBridge BEH C18 column (elute A: H_2O , 0.1% HCOOH ; elute B: Acetonitrile, 0.1% HCOOH). The peaks in 254 nm were integrated and plotted as a function of AA concentrations to make calibration curves (Fig. S22). Then, the collected L-aspartic acid and L-asparagine from the coacervate solutions were treated and analyzed following the same procedure, and the concentrations in the supernatant were determined based on the calibration curves. The concentrations of L-aspartic acid and L-asparagine in coacervates were calculated as $c_{\text{coacervate}} = (c_{\text{solution}} * v_{\text{solution}} - c_{\text{supernatant}} * v_{\text{supernatant}}) / v_{\text{coacervate}}$. Then, the partitioning efficiency was calculated as $K_p = c_{\text{coacervate}} / c_{\text{supernatant}}$. Three samples were analyzed for each amino acid, and the average value was presented.

Determination of the enzymatic activity of ASP-K72

The enzymatic activity of ASP-K72 was determined by following the instructions provided by the supplier. Briefly, L-asparagine (100 μL , 40 mM), ASP-K72 (100 μL , 1 $\mu\text{g mL}^{-1}$) and phosphate buffer (50 mM, pH 7.4) were mixed and incubated at 37 °C for 10 min. Then, CCl_3COOH (50 μL) was added to terminate the reaction. Afterward, 100 μL of the solution was mixed with 100 μL of Nessler reagent, and the absorption of the solution at 450 nm was recorded with a BioTek Cytation 3-microplate reader in a 96-well plate at room temperature. To determine the concentration of NH_3 produced by ASP-K72, a calibration curve was plotted by reacting Nessler's reagent (100 μL) with

100 μL NH_4Cl of different concentrations (2, 1.5, 0.5, 0.25, 0 mM), and the absorption at 450 nm was recorded (Fig. S11d).

Determination of ASP-K72 activity in the presence of L-aspartic acid followed the same procedure. ASP-K72 concentration was fixed at 1 $\mu\text{g mL}^{-1}$ while L-aspartic acid concentration was varied (1, 3, 5, 7, 9, 11, 13, 15, 17 and 20 mM).

Observation of static and transient vacuolation

The setup is based on the previous report and depicted in Fig. S2²⁸. In a typical experimental procedure, the coacervate was preassembled in a tube, and 5 μL of the solution was placed on a glass slide and covered with a covering glass. Then, 1 μL of the guest solution (K72, GFP30 or AAs) in the same buffer was added, and the slide was directly observed focusing on the area close to the injection point.

Fluorescence recovery after photobleaching (FRAP) measurement

FRAP measurements were performed using a laser scanning confocal microscope (OLYMPUS FV3000) equipped with a temperature-controlling block. Coacervate droplets or rims were prepared by using the setup depicted in Fig. S2. A selected region of interest in the droplets or rims was bleached using a 0.5 s pulse of the 488 nm laser line at full power. Afterward, the fluorescence intensity from the bleached region was monitored until the recovery was complete. For analysis, FRAP recovery curves were fitted using the imageJ plugin FRAP PROFILER.

Determination of the L-asparagine-induced in situ pH change within K72-ASP/GFP30

ASP-K72 and pHrodo™ Red were first mixed, and GFP30 was then added to produce ASP-K72/GFP30 coacervates with pHrodo™ Red homogeneously distributed across the droplets ($c_{\text{positive charge}} = c_{\text{negative charge}} = 3 \text{ mM}$; 1× pHrodo™ Red as suggested by the supplier). The samples were observed by laser confocal microscopy. After determining the plane of focus, the parameters (such as the laser intensity and background deduction) that may affect the fluorescence intensity were fixed. Then, L-asparagine was gently added as aforementioned, and the XYT scanning mode was used for real-time recording of the samples ($\lambda_{\text{ex}} = 488 \text{ nm}$ for GFP30 and $\lambda_{\text{ex}} = 561 \text{ nm}$ for pHrodo™ Red). The evolution of the fluorescence intensity was recorded, and the mean fluorescence intensity of GFP30 and pHrodo™ Red in droplets was analyzed by imageJ.

Statistical Analysis

All of the statistically significant differences were determined using Student's *t*-test. Significance was set to * $p < 0.05$, ** $p < 0.01$, *** $p < 0.001$ and **** $p < 0.0001$.

Reporting summary

Further information on research design is available in the Nature Portfolio Reporting Summary linked to this article.

Data availability

The data that support the findings of this study have been deposited in Figshare under accession code (10.6084/m9.figshare.29323670) and are available in the Supplementary Information. Any requests for information can be directed to and will be fulfilled by the corresponding authors. Source data are provided in this paper. Source data are provided with this paper.

References

- Hyman, A. A., Weber, C. A. & Frank, J. Liquid-liquid phase separation in biology. *Annu. Rev. Cell Dev. Biol.* **30**, 39–58 (2014).
- Banani, S. F., Lee, H. O., Hyman, A. A. & Rosen, M. K. Biomolecular condensates: organizers of cellular biochemistry. *Nat. Rev. Mol. Cell Biol.* **18**, 285–298 (2017).

3. Lyon, A. S., Peeples, W. B. & Rosen, M. K. A framework for understanding the functions of biomolecular condensates across scales. *Nat. Rev. Mol. Cell Biol.* **22**, 215–235 (2021).
4. Brangwynne, C. P. et al. Germline P granules are liquid droplets that localize by controlled dissolution/condensation. *Science* **324**, 1729–1732 (2009).
5. Wippich, F. et al. Dual specificity kinase DYRK3 couples stress granule condensation/dissolution to mTORC1 signaling. *Cell* **152**, 791–805 (2013).
6. Wang, J. T. et al. Regulation of RNA granule dynamics by phosphorylation of serine-rich, intrinsically disordered proteins in *C. elegans*. *eLife* **3**, e04591 (2014).
7. Mitrea, D. M. & Kriwacki, R. W. Phase separation in biology; functional organization of a higher order. *Cell Commun. Signal.* **14**, 1 (2016).
8. Brangwynne, C. P., Mitchison, T. J. & Hyman, A. A. Active liquid-like behavior of nucleoli determines their size and shape in *Xenopus laevis* oocytes. *Proc. Natl. Acad. Sci. USA* **108**, 4334–4339 (2011).
9. Jain, S. et al. ATPase-modulated stress granules contain a diverse proteome and substructure. *Cell* **164**, 487–498 (2016).
10. Feric, M. et al. Coexisting liquid phases underlie nucleolar sub-compartments. *Cell* **165**, 1686–1697 (2016).
11. Sanders, D. W. et al. Competing protein-RNA interaction networks control multiphase intracellular organization. *Cell* **181**, 306–324 (2020).
12. Kim, T. H. et al. Phospho-dependent phase separation of FMRP and CAPRIN1 recapitulates regulation of translation and deadenylation. *Science* **365**, 825–829 (2019).
13. Putnam, A., Cassani, M., Smith, J. & Seydoux, G. A gel phase promotes condensation of liquid P granules in *Caenorhabditis elegans* embryos. *Nat. Struct. Mol. Biol.* **26**, 220–226 (2019).
14. Buchan, J. R. & Parker, R. Eukaryotic stress granules: the ins and outs of translation. *Mol. Cell* **36**, 932–941 (2009).
15. Brengues, M., Teixeira, D. & Parker, R. Movement of eukaryotic mRNAs between polysomes and cytoplasmic processing bodies. *Science* **310**, 486–489 (2005).
16. Niewidok, B. et al. Single-molecule imaging reveals dynamic biphasic partition of RNA-binding proteins in stress granules. *J. Cell Biol.* **217**, 1303–1318 (2018).
17. Caragine, C. M., Haley, S. C. & Zidovska, A. Nucleolar dynamics and interactions with nucleoplasm in living cells. *eLife* **8**, e47533 (2019).
18. Lewis, W. H. Nucleolar vacuoles in living normal and malignant fibroblasts. *Cancer Res.* **3**, 531–536 (1943).
19. Arkov, A. L., Wang, J. S., Ramos, A. & Lehmann, R. The role of Tudor domains in germline development and polar granule architecture. *Development* **133**, 4053–4062 (2006).
20. Kistler, K. E. et al. Phase transitioned nuclear Oskar promotes cell division of *Drosophila* primordial germ cells. *eLife* **7**, e37949 (2018).
21. Yu, H. et al. HSP70 chaperones RNA-free TDP-43 into anisotropic intranuclear liquid spherical shells. *Science* **371**, eabb4309 (2021).
22. Shin, Y. & Brangwynne, C. P. Liquid phase condensation in cell physiology and disease. *Science* **357**, eaaf4382 (2017).
23. Alberti, S., Gladfelter, A. & Mittag, T. Considerations and challenges in studying liquid-liquid phase separation and biomolecular condensates. *Cell* **176**, 419–434 (2019).
24. Nakashima, K. K., Vibhute, M. A. & Spruijt, E. Biomolecular chemistry in liquid phase separated compartments. *Front. Mol. Biosci.* **6**, 21 (2019).
25. Sing, C. E. & Perry, S. L. Recent progress in the science of complex coacervation. *Soft Matter* **16**, 2885–2914 (2020).
26. Yewdall, N. A., André, A. A. M., Lu, T. & Spruijt, E. Coacervates as models of membraneless organelles. *Curr. Opin. Colloid Interface Sci.* **52**, 101416 (2021).
27. Wang, J., Abbas, M., Wang, J. & Spruijt, E. Selective amide bond formation in redox-active coacervate protocells. *Nat. Commun.* **14**, 8492 (2023).
28. te Brinke, E. et al. Dissipative adaptation in driven self-assembly leading to self-dividing fibrils. *Nat. Nanotechnol.* **13**, 849–855 (2018).
29. Donau, C. et al. Active coacervate droplets as a model for membraneless organelles and protocells. *Nat. Commun.* **11**, 5167 (2020).
30. Deng, J. & Walther, A. Programmable and chemically fueled DNA coacervates by transient liquid-liquid phase separation. *Chem* **6**, 3329–3343 (2020).
31. Reineke, L. C. et al. Casein kinase 2 is linked to stress granule dynamics through phosphorylation of the stress granule nucleating protein G3BP1. *Mol. Cell. Biol.* **37**, e00596–e00616 (2017).
32. Gomes, E. & Shorter, J. The molecular language of membraneless organelles. *J. Biol. Chem.* **294**, 7115–7127 (2019).
33. Saito, M. et al. Acetylation of intrinsically disordered regions regulates phase separation. *Nat. Chem. Biol.* **15**, 51–61 (2019).
34. Merindol, R. & Walther, A. Materials learning from life: concepts for active, adaptive and autonomous molecular systems. *Chem. Soc. Rev.* **46**, 5588–5619 (2017).
35. Walther, A. Viewpoint: From responsive to adaptive and interactive materials and materials systems: a roadmap. *Adv. Mater.* **32**, e1905111 (2020).
36. Liu, Q. et al. DNA-based dissipative assembly toward nanoarchitectonics. *Adv. Funct. Mater.* **32**, 2201196 (2022).
37. Kaur, T. et al. Sequence-encoded and composition-dependent protein-RNA interactions control multiphase condensate morphologies. *Nat. Commun.* **12**, 872 (2021).
38. Lu, T. & Spruijt, E. Multiphase complex coacervate droplets. *J. Am. Chem. Soc.* **142**, 2905–2914 (2020).
39. Donau, C., Späth, F., Stasi, M., Bergmann, A. M. & Boekhoven, J. Phase transitions in chemically fueled, multiphase complex coacervate droplets. *Angew. Chem. Int. Ed.* **134**, e202211905 (2022).
40. Fisher, R. S. & Elbaum-Garfinkle, S. Tunable multiphase dynamics of arginine and lysine liquid condensates. *Nat. Commun.* **11**, 4628 (2020).
41. Choi, S., Meyer, M. O., Bevilacqua, P. C. & Keating, C. D. Phase-specific RNA accumulation and duplex thermodynamics in multiphase coacervate models for membraneless organelles. *Nat. Chem.* **14**, 1110–1117 (2022).
42. Moreau, N. G., Martin, N., Gobbo, P., Tang, T.-Y. D. & Mann, S. Spontaneous membrane-less multi-compartmentalization via aqueous two-phase separation in complex coacervate micro-droplets. *Chem. Commun.* **56**, 12717–12720 (2020).
43. Yin, Y. et al. Non-equilibrium behaviour in coacervate-based protocells under electric-field-induced excitation. *Nat. Commun.* **7**, 10658 (2016).
44. Banerjee, P. R., Milin, A. N., Moosa, M. M., Onuchic, P. L. & Deniz, A. A. Reentrant phase transition drives dynamic substructure formation in ribonucleoprotein droplets. *Angew. Chem. Int. Ed.* **56**, 11354–11359 (2017).
45. Alshareedah, I., Moosa, M. M., Raju, M., Potoyan, D. A. & Banerjee, P. R. Phase transition of RNA-protein complexes into ordered hollow condensates. *Proc. Natl. Acad. Sci. USA* **117**, 15650–15658 (2020).
46. Yin, Z., Tian, L., Patil, A. J., Li, M. & Mann, S. Spontaneous membraneless organization in a silk-based coacervate protocell model. *Angew. Chem. Int. Ed.* **61**, e202202302 (2022).
47. Yin, Z., Gao, N., Xu, C., Li, M. & Mann, S. Autonomic integration in nested protocell communities. *J. Am. Chem. Soc.* **145**, 14727–14736 (2023).
48. Erkamp, N. A. et al. Spatially non-uniform condensates emerge from dynamically arrested phase separation. *Nat. Commun.* **14**, 684 (2023).
49. Zhang, Y. et al. Osmotic-induced reconfiguration and activation in membraneless coacervate-based protocells. *J. Am. Chem. Soc.* **145**, 10396–10403 (2023).
50. Saleh, O. A., Jeon, B.-J. & Liedl, T. Enzymatic degradation of liquid droplets of DNA is modulated near the phase boundary. *Proc. Natl. Acad. Sci. USA* **117**, 16160–16166 (2020).

51. Saleh, O. A., Wilken, S., Squires, T. M. & Liedl, T. Vacuole dynamics and popping-based motility in liquid droplets of DNA. *Nat. Commun.* **14**, 3574 (2023).
52. Alshareedah, I. et al. Interplay between short-range attraction and long-range repulsion controls reentrant liquid condensation of ribonucleoprotein-RNA complexes. *J. Am. Chem. Soc.* **141**, 14593–14602 (2019).
53. Liu, W., Deng, J., Song, S., Sethi, S. & Walther, A. A facile DNA coacervate platform for engineering wetting, engulfment, fusion and transient behavior. *Commun. Chem.* **7**, 100 (2024).
54. Bergmann, A. M. et al. Liquid spherical shells are a non-equilibrium steady state of active droplets. *Nat. Commun.* **14**, 6552 (2023).
55. Liu, J., Feng, R. & Chau, Y. Large-sized but ready to enter: Micron-sized liquid droplets for versatile intracellular delivery. *Matter* **5**, 1637–1639 (2022).
56. Ma, C. et al. Ultra-strong bio-glue from genetically engineered polypeptides. *Nat. Commun.* **12**, 3613 (2021).
57. Lawrence, M. S., Phillips, K. J. & Liu, D. R. Supercharging proteins can impart unusual resilience. *J. Am. Chem. Soc.* **129**, 10110–10112 (2007).
58. Ruff, K. M., Dar, F. & Pappu, R. V. Ligand effects on phase separation of multivalent macromolecules. *Proc. Natl. Acad. Sci. USA* **118**, e2017184118 (2021).
59. Koga, S., Williams, D. S., Perriman, A. W. & Mann, S. Peptide–nucleotide microdroplets as a step towards a membrane-free protocell model. *Nat. Chem.* **3**, 720–724 (2011).
60. Frankel, E. A., Bevilacqua, P. C. & Keating, C. D. Polyamine/nucleotide coacervates provide strong compartmentalization of Mg^{2+} , nucleotides, and RNA. *Langmuir* **32**, 2041–2049 (2016).
61. Zhu, L., Pan, Y., Hua, Z., Liu, Y. & Zhang, X. Ionic effect on the microenvironment of biomolecular condensates. *J. Am. Chem. Soc.* **146**, 14307–14317 (2024).
62. Liu, W., Lupfer, C., Samanta, A., Sarkar, A. & Walther, A. Switchable hydrophobic pockets in DNA protocells enhance chemical conversion. *J. Am. Chem. Soc.* **145**, 7090–7094 (2023).
63. Shen, Y. et al. Biomolecular condensates undergo a generic shear-mediated liquid-to-solid transition. *Nat. Nanotechnol.* **15**, 841–847 (2020).
64. El-Naggar, N. E.-A. & El-Shweihy, N. M. Bioprocess development for L-asparaginase production by *Streptomyces rochei*, purification and in-vitro efficacy against various human carcinoma cell lines. *Sci. Rep.* **10**, 7942 (2020).
65. Talluri, V. P. et al. L-Asparaginase delivery systems targeted to minimize its side-effects. *Adv. Colloid Interface Sci.* **316**, 102915 (2023).
66. Heinen, L., Heuser, T., Steinschulte, A. & Walther, A. Antagonistic enzymes in a biocatalytic pH feedback system program autonomous DNA hydrogel life cycles. *Nano Lett.* **17**, 4989–4995 (2017).
67. Deng, J., Bezold, D., Jessen, H. J. & Walther, A. Multiple light control mechanisms in ATP-fueled non-equilibrium DNA systems. *Angew. Chem. Int. Ed.* **59**, 12084–12092 (2020).
68. Ragazzon, G. & Prins, L. J. Energy consumption in chemical fuel-driven self-assembly. *Nat. Nanotechnol.* **13**, 882–889 (2018).
69. Amano, S., Borsley, S., Leigh, D. A. & Sun, Z. Chemical engines: driving systems away from equilibrium through catalyst reaction cycles. *Nat. Nanotechnol.* **16**, 1057–1067 (2021).
70. Weißenfels, M., Gemen, J. & Klajn, R. Dissipative self-assembly: fueling with chemicals versus light. *Chem* **7**, 23–37 (2021).
71. Nakashima, K. K., van Haren, M. H. I., André, A. A. M., Robu, I. & Spruijt, E. Active coacervate droplets are protocells that grow and resist Ostwald ripening. *Nat. Commun.* **12**, 3819 (2020).

Acknowledgements

We acknowledge the funding from the Zhejiang Provincial Natural Science Foundation for Distinguished Young Scholar (LR23B030001), the National Nature Science Foundation of China (No. 22277018, 22278264, 22372049, 22205047) and Wenzhou Institute, University of Chinese Academy of Sciences (No. WIUCASQD2020015, WIUCASQD2022006, WIUCASQD2021048).

Author contributions

L.Z. and N.-N.D. supervised the research. L.Z., Z.L. and Q.L. designed the experiments. Z.L. and H.D. expressed and purified the proteins. Z.M. and Q.-H.Z. contributed to the confocal fluorescence microscopy measurement and data analysis. Z.L. prepared all the coacervates and performed the relevant studies. Q.L. and Z.L. wrote the manuscript with input from all authors.

Competing interests

The authors declare no competing interests.

Additional information

Supplementary information The online version contains supplementary material available at <https://doi.org/10.1038/s41467-025-61340-w>.

Correspondence and requests for materials should be addressed to Nan-Nan Deng or Lifei Zheng.

Peer review information *Nature Communications* thanks Andreas Walther and the other, anonymous, reviewers for their contribution to the peer review of this work. A peer review file is available.

Reprints and permissions information is available at <http://www.nature.com/reprints>

Publisher's note Springer Nature remains neutral with regard to jurisdictional claims in published maps and institutional affiliations.

Open Access This article is licensed under a Creative Commons Attribution-NonCommercial-NoDerivatives 4.0 International License, which permits any non-commercial use, sharing, distribution and reproduction in any medium or format, as long as you give appropriate credit to the original author(s) and the source, provide a link to the Creative Commons licence, and indicate if you modified the licensed material. You do not have permission under this licence to share adapted material derived from this article or parts of it. The images or other third party material in this article are included in the article's Creative Commons licence, unless indicated otherwise in a credit line to the material. If material is not included in the article's Creative Commons licence and your intended use is not permitted by statutory regulation or exceeds the permitted use, you will need to obtain permission directly from the copyright holder. To view a copy of this licence, visit <http://creativecommons.org/licenses/by-nc-nd/4.0/>.

© The Author(s) 2025